Received May 31, 2020, accepted June 15, 2020, date of publication June 19, 2020, date of current version July 1, 2020.

Digital Object Identifier 10.1109/ACCESS.2020.3003654

IGBT Junction Temperature Measurement Under Active-Short-Circuit and Locked-Rotor Modes in New Energy Vehicles

YUAN ZHU[1], MINGKANG XIAO[1], XIEZU SU[1], KE LU[1], ZHIHONG WU[1], (Member, IEEE), AND GANG YANG[2]

[1]School of Automotive Studies, Tongji University, Shanghai 201800, China
[2]School of Electronics and Information Engineering, Tongji University, Shanghai 201800, China

Corresponding author: Xiezu Su (suxiezu@126.com)

This work was supported in part by the National Key Research and Development Program of China under Grant 2016YFB0100804.

ABSTRACT Active-short-circuit and locked-rotor modes are common abnormal operations in new energy vehicles. The IGBT junction temperature measurement for these two operating conditions is a challenging problem due to the unexpected large current and the asymmetric operation of semiconductor chips. In addition, different cooling flow rates have a significant influence on the heat dissipation, which will also have an impact on the building of the thermal model. Based on these difficulties, a modified Foster thermal network under active-short-circuit and locked-rotor modes has been presented considering different cooling conditions. The power loss models of the semiconductor chip under abnormal conditions are developed and a modified Foster thermal network based on the NTC temperature sensor is proposed. The model can be adapted to different cooling conditions since the thermal impedance fluctuates slightly at different cooling flow rates. The proposed thermal model is verified with inverter application under active-short-circuit and locked-rotor modes and the experimental performance shows good accuracy compared with the infrared camera measurement results.

INDEX TERMS Insulated gate bipolar transistors (IGBTs), active short circuit (ASC) mode, locked-rotor mode, thermal models.

I. INTRODUCTION

The junction temperature measurement of insulated gate bipolar transistors(IGBTs) is one of the main problems affecting the performances and reliability of power converters in electric drive system of new energy vehicles [1]. The accurate junction temperature information is desired for reliability prediction and indication of the IGBT failures [2]–[4]. It can be also used to realize active thermal control for high-power inverters [3] and real-time aging monitoring [5], [6].

There have been many methods to predict the IGBT junction temperature, such as optical-based, physical contact-based, temperature sensitive electrical parameter(TSEP)-based [7]–[12], and thermal model-based [13]–[15]. The first two methods are usually not applicable due to the substantial modifications to the standard power module packaging and are therefore used to validate the temperature estimation accuracy of other methods [16]. TSEP-based approach can establish the relationship between the junction temperature and observable electrical parameters, such as: peak gate current [7], forward voltage [8], flat-band voltage [9], on-state voltage [10],turn-off delay time [11], and short-circuit current [12]. A good linear relationship with temperature can be found in the above mentioned TSEP methods with good temperature estimation accuracy. However, considering the practical application in automobile industries, TSEPs have shown some weakness compared with the establishment of equivalent thermal model, since the measurement of observable electrical parameters depends on the additional devices, ending up in a large cost pressure and the lower reliability.

Generally, two groups of thermal model can be found in the literature, including the thermal simulation, such as finite-element method (FEM) [14], [17] and thermal networks, such as Cauer or Foster equivalent thermal models [18]–[20]. In [14], an updated Cauer thermal model is proposed under short-circuit and overloads, and FEM thermal simulations

The associate editor coordinating the review of this manuscript and approving it for publication was Alfeu J. Sguarezi Filho.

are applied to identify the temperature-dependent thermal impedance. The effectiveness of the model is validated with a black-painted open IGBT module. A four-order Cauer network is presented using the junction temperature cooling curve with the advantages of not knowing the power loss information of IGBT [18], [19]. The Cauer model is built based on the geometry and physical property of the IGBT modules and it is considered to be a relatively accurate model to predict the thermal behaviors. However, the Cauer model requires large computational resources and the online temperature estimation is hardly to implement, which is not feasible in real-time automobile embedded software. Therefore, the Foster thermal model is chosen as a better alternative to measure the junction temperature.

In the past research, more attention has been paid to thermal stresses on IGBT modules under the normal operating applications. However, the common abnormal operation in electric drive system such as active-short-circuit (ASC) [21] and locked-rotor(LR) modes [22] should be investigated, since large energies will be involved and the operations can drive the semiconductor chips into destruction immediately when reaching the thermal limit.

The short-circuit operation is caused when one IGBT is conducting, and the opposite is switched on, which is different from the ASC operation mechanism [6]. With respect to the ASC mode, it serves as a protection mechanism according to the functional safety standards for vehicle ISO 26262 [23], [24]. Three high-side IGBTs or three low-side IGBTs are switched on during the ASC operation and the three phases of the motor are short circuited via the high-side IGBTs or the low-side IGBTs, respectively [21]. In this case, either the high-side or low-side IGBTs are switched, resulting in asymmetric operation of the inverter. LR operation occurs when the vehicle starts on the slope, or is driven with the brake on. Under the LR condition, the motor rotor keeps stationary and the LR current in stator windings can reach seven times of the rated current due to the absence of back electromotive force [22], [25]. As a result, a huge current flows through the IGBTs and the chips will be over heated severely if left uncontrolled. Therefore, it can be concluded that the power loss and thermal stress are indicated different when compared with normal operation.

Thus, the real-time knowledge of the junction temperature under such abnormal modes is of vital importance for a reliable operation. However, as far as we know, few literatures focus on the problems regarding the junction temperature estimation under the LR and ASC conditions during the operation of electric drive system. In addition, when the inverter operates in these two abnormal modes, the coolant flow rate will be adjusted to accelerate the heat dissipation. As for the traditional Foster network, the thermal impedances change with the flow rate. The thermal impedances should be measured under different flow rates, which leads to too much measurement pressure [15]. Based on the above problems, this paper proposes a modified Foster thermal network based on the negative temperature coefficient (NTC) temperature sensor to measure the IGBT junction temperature under LR and ASC modes. The contribution of this paper is concluded as follow:

1) Few researchers focus on the abnormal mode in electrical drive systems for new energy vehicles, and the junction temperature of abnormal operation is different from that of normal operation, especially in power loss calculation. Therefore, this paper focuses on the junction temperature prediction under abnormal modes in new energy vehicles and studies the power loss under the abnormal operation in detail.

2) The paper proposed a modified Foster thermal model, which is independent of the flow rate and shows a good temperature prediction accuracy under abnormal conditions. The proposed thermal model is the improvements of the traditional Foster thermal model. When the traditional model is adopted, the thermal impedances should be calibrated under different flow rates.

3) Furthermore, the proposed Foster thermal model has the advantages of simple mathematical calculation and easy digital discretization, which is easy to realize the real-time junction temperature prediction in practical engineering applications.

This paper is organized as follows. Section II presents the power losses models under the LR and ASC conditions. In Section III, a modified Foster thermal network based on the NTC temperature sensor is proposed under different cooling conditions. Test setup and experimental results are presented in Section IV. Conclusion is drawn in Section V.

II. POWER LOSS MODEL

The power loss of IGBT and FWD is the main heat source resulting in overheating of semiconductor devices. The universal power loss model is not applicable to the abnormal operation, so the power losses under LR and ASC modes are studied in detail as follow.

A. UNDER ROTOR-LOCKED CONDITION

Under the rotor-locked condition, the current output is the direct current and not the periodic sine current. In this case, the original IGBT and free-wheeling diode(FWD) power loss models are no longer applicable and need to be restudied. It is noted that the direct current is still modulated by space vector pulse width modulation(SVPWM) algorithm under LR condition, and the sum of three-phase currents is still equal to 0.

Fig.1 illustrates the eight basic voltage space vectors which are modulated to obtain the target voltage vector based on SVPWM. Since the motor rotor position no longer changes, it can be assumed that the rotor position is in the first sector and the current direction is positive. Therefore, the voltage vector is composed of the basic vectors 100, 110, 000, and 111. The target vector satisfies the volt-second equilibrium principle, so (1) and (2) are obtained.

$$TU_s = \frac{T_0}{2}U_{000} + T_aU_{100} + T_bU_{110} + \frac{T_0}{2}U_{111} \quad (1)$$

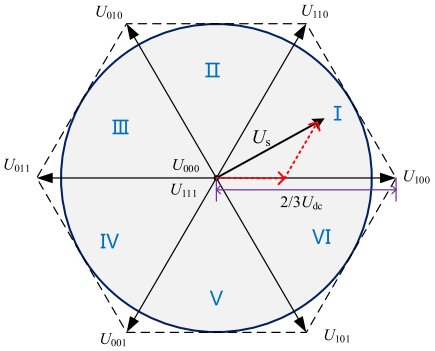

FIGURE 1. Diagram of the voltage space vector.

$$T = T_0 + T_a + T_b \tag{2}$$

where T represents the switching period; U_s is the voltage space vector; T_a, T_b, T_0 are the operating period of the basic space vector U_{100}, U_{110}, and the two zero vector, respectively.

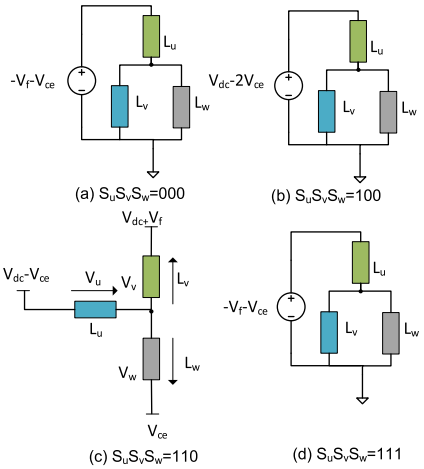

FIGURE 2. Equivalent circuit under four basic voltage vectors in the first sector.

Fig.2 shows the equivalent circuit under four basic voltage vector U_{100}, U_{110}, U_{111} and U_{000} in the first sector. The corresponding current growth rates are k_1, k_2, k_3 and k_4, respectively, which are indicated as

$$\begin{aligned} k_1 &= \frac{2V_{dc} - 4V_{ce}}{3L_u} \\ k_2 &= \frac{(V_{dc} - V_f) - 3V_{ce}}{3L_u} \\ k_3 = k_4 &= \frac{-2V_f - 2V_{ce}}{3L_u} \end{aligned} \tag{3}$$

where V_{dc} indicates the dc bus voltage; V_{ce} and V_f are the on-state voltage drops of IGBT and FWD respectively; L_u, L_v and L_w represent the three-phase impedance of the motor respectively.

According to the actual physical parameters of semiconductor chips used in electric vehicle inverter, the high voltage bus voltage V_{dc} is around 400V, whereas V_{ce} and V_f are usually only around 1V. Therefore, the relationships of the current growth rate are expressed by the following formulas.

$$\begin{aligned} k_1 &\cong 2k_2 \\ k_1 &\gg k_3 \\ k_1 &\gg k_4 \end{aligned} \tag{4}$$

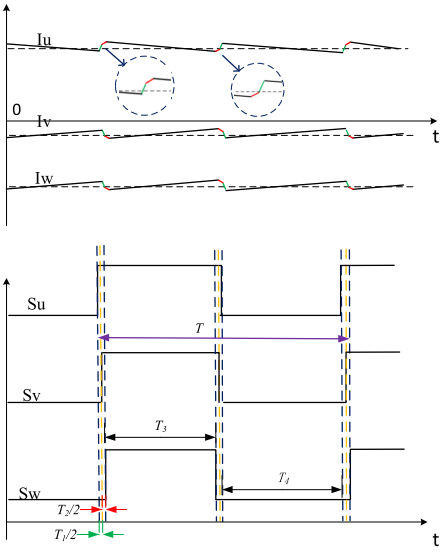

FIGURE 3. Modulation principle of dc current based on seven-stage SVPWM.

Fig. 3 shows the modulation principle of direct current based on seven-stage SVPWM. Under the LR condition, the current period has no relationship with the motor speed. The phase current is a unipolar pulse current, which may be positive or negative with the average direct current. Furthermore, the PWM ripple is superimposed on direct current due to PWM modulation.

Since the locked-rotor current is the direct current, the current growth is 0 both in the first half period and in the other half period, as shown in (5) and (6).

$$0 = k_1\frac{T_1}{2} + k_2\frac{T_2}{2} + k_3\frac{T_3}{2} \tag{5}$$

$$0 = k_1\frac{T_1}{2} + k_2\frac{T_2}{2} + k_4\frac{T_4}{2} \tag{6}$$

Considering the current growth rate, the operating period of four basic voltage vectors can be obtained as follows

$$(T_1 + T_2) \ll T_3$$

$$(T_1 + T_2) \ll T_4 \tag{7}$$

$$T_1 + T_2 + T_3 + T_4 = T \tag{8}$$

$$T_3 = T_4 \tag{9}$$

According to (7) to (9), the operating period of the two basic zero voltage vectors is dominant, whereas the time for two non-zero basic vectors is negligible. As a result, the duty ratio of the switching period is about 50%, which provides the basis for the calculation of IGBT modules loss under zero vector.

Since the IGBT switch is still modulated by PWM under LR condition, IGBT power loss $P_{loss}(IGBT)$ and FWD power

loss $P_{loss}(FWD)$ are composed of switching loss and conduction loss, respectively. The power loss calculation is expressed in (10).

$$\begin{aligned} P_{cond}(IGBT) &= V_{ce} I_{ref} D_{sw} \\ P_{sw}(IGBT) &= (E_{on} + E_{off}) \times f_{sw} \\ P_{loss}(IGBT) &= P_{cond}(IGBT) + P_{sw}(IGBT) \\ P_{cond}(FWD) &= V_f I_{ref} \times (1 - D_{sw}) \\ P_{sw}(FWD) &= (E_{rr}) \times f_{sw} \\ P_{loss}(FWD) &= P_{cond}(FWD) + P_{sw}(FWD) \end{aligned} \tag{10}$$

where E_{on}, E_{off} and E_{rr} represent the turn-on loss and turn-off loss of IGBT, and the switching energy loss of FWD, respectively. $P_{cond}\,(IGBT)$, $P_{sw}\,(IGBT)$, $P_{cond}\,(FWD)$ and $P_{sw}\,(FWD)$ are the conduction loss and switching loss of IGBT and FWD respectively. I_{ref}, D_{sw} and f_{sw} represent the locked-rotor current, duty ratio and switching frequency, respectively.

B. UNDER ACTIVE-SHORT-CIRCUIT CONDITION

The ASC operation is no longer modulated by SVPWM algorithm, and either the upper IGBT modules or lower IGBT modules are switched.

Since the motor three-phase windings are symmetrically distributed and the back-EMF is in sinusoidal form, the current through the three upper switches can be expressed as follows.

$$\begin{aligned} i_u &= I_p \cos(\theta) \\ i_v &= I_p \cos\left(\theta + \frac{2\pi}{3}\right) \\ i_w &= I_p \cos\left(\theta - \frac{2\pi}{3}\right) \end{aligned} \tag{11}$$

Taking U phase upper switch as an example, the positive-cycle phase current flows through IGBT and the negative-cycle phase current flows through the reverse parallel FWD. Thus, IGBT average conduction loss in a whole current cycle can be calculated as follows.

$$P_{igbt} = \frac{1}{2\pi} \int_{-\frac{\pi}{2}}^{\frac{\pi}{2}} I_p \cos(\theta) \times \left(V_{ceo} + r_{ce} I_p \cos(\theta)\right) d\theta \tag{12}$$

Equation (12) can be simplified as

$$P_{igbt} = \frac{1}{\pi} v_{ceo} I_p + \frac{1}{4} r_{ce} I_p^2 \tag{13}$$

Similarly, the FWD conduction loss can be calculated as

$$P_{fwd} = \frac{1}{2\pi} \int_{\frac{\pi}{2}}^{\frac{3\pi}{2}} (-I_p) \times \cos(\theta) \times \left(V_f - r_f I_p \cos(\theta)\right) d\theta \tag{14}$$

Equation (25) can be simplified as

$$P_{fwd} = \frac{1}{\pi} v_f I_p + \frac{1}{4} r_f I_p^2 \tag{15}$$

where V_{ceo} and r_{ce} represent on-state voltage drop and conduction resistance of IGBT; V_f and r_f are on-state voltage drop and conduction resistance of FWD. I_p is the amplitude of the sinusoidal current.

For the calculation of conduction loss of IGBT and FWD, sinusoidal current amplitude I_p is unknown. Since the current is not the result of current loop control, it cannot be obtained from target current i_d and i_q. The current acquisition depends on the current sensor. The three-phase symmetrical current can be real-time sampled by the microprocessor, so the current vector can be calculated as

$$\begin{aligned} \overrightarrow{i_{ref}} &= \overrightarrow{i_u} + \overrightarrow{i_v} + \overrightarrow{i_w} = I_u e^{j0} + I_v e^{-j\frac{2\pi}{3}} + I_w e^{j\frac{2\pi}{3}} \\ &= \left(I_u - \frac{1}{2} I_v - \frac{1}{2} I_w\right) + j\left(\frac{\sqrt{3}}{2}(-I_v + I_w)\right) \end{aligned} \tag{16}$$

The sinusoidal current amplitude can be obtained as

$$\begin{aligned} \left|\overrightarrow{I_{ref}}\right| &= \sqrt{\left(I_u - \frac{1}{2} I_v - \frac{1}{2} I_w\right)^2 + \left(\frac{\sqrt{3}}{2}(-I_v + I_w)\right)^2} \\ &= \frac{3}{2}\sqrt{(I_u)^2 + \frac{1}{3}(-I_v + I_w)^2} \end{aligned} \tag{17}$$

Furthermore, the synthesis vector of three phase sinusoidal current is calculated:

$$\begin{aligned} \overrightarrow{i_{ref}} &= \overrightarrow{i_u} + \overrightarrow{i_v} + \overrightarrow{i_w} \\ &= I_p \cos(\theta)\, e^{j0} + I_p \cos\left(\theta - \frac{2\pi}{3}\right) e^{-j\frac{2\pi}{3}} \\ &\quad + I_p \cos\left(\theta + \frac{2\pi}{3}\right) e^{j\frac{2\pi}{3}} = \frac{3}{2} I_p e^{-j\theta} \end{aligned} \tag{18}$$

According to (17) and (18), it can be obtained that

$$I_p = \sqrt{(I_u)^2 + \frac{1}{3}(-I_v + I_w)^2} \tag{19}$$

It should be noted that IGBT has only conduction loss and no switching loss, since the IGBT switching state is constant ON without PWM modulation under ASC condition. Furthermore, FWD will be switched passively as the current direction changes and its switching loss needs to be calculated. However, FWD is switched on and off at zero current, so there is only conduction loss for FWD under ASC mode.

III. FOSTER EQUIVALENT THERMAL MODEL

The Foster thermal model is adopted due to simple mathematical calculation and easy digital discretization.

A. TRADITIONAL THERMAL MODEL

The traditional thermal model shown in Fig. 4(a) is the heat transfer model based on the coolant temperature at the inlet of the inverter, and the mathematical model is shown in (20). This method requires the knowledge of coolant temperature. However, in practical application, the temperature sensors are usually not installed in the cooling loop considering the simplify and reliability of the system. In this case, the coolant temperature is estimated by means of the thermal model

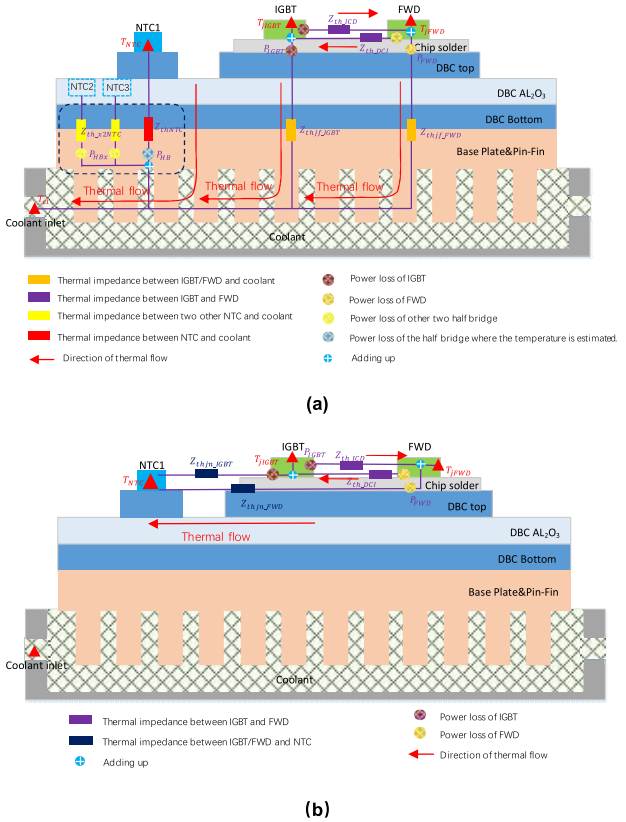

FIGURE 4. Thermal impedance network model (a) traditional thermal model (b) proposed thermal model.

between the NTC and coolant, since the temperature of equipped NTC temperature sensor can be real-time obtained. The coolant temperature can be obtained according to (21) based on the NTC temperature.

$$\begin{aligned} T_{jIGBT}(t) &= T_{cl}(t) + Z_{thjf\_IGBT}(t)\,P_{IGBT}(t) \\ &\quad + Z_{th\_DCI}(t)P_{FWD}(t) \\ T_{jFWD}(t) &= T_{cl}(t) + Z_{thjf\_FWD}(t)\,P_{FWD}(t) \\ &\quad + Z_{th\_ICD}(t)P_{IGBT}(t) \end{aligned} \tag{20}$$

$$\begin{aligned} T_{cl}(t) &= T_{NTC}(t) - Z_{th\_x2NTC}(t)\,P_{HBx}(t) \\ &\quad - Z_{th\_NTC}(t)\,P_{HB}(t) \end{aligned} \tag{21}$$

where $T_{jIGBT}(t)$, $T_{jFWD}(t)$, $T_{cl}(t)$ and $T_{NTC}(t)$ represent the junction temperature of IGBT, the junction temperature of FWD, coolant temperature and NTC temperature, respectively; $P_{IGBT}(t)$, $P_{FWD}(t)$ and $P_{HB}(t)$ represent the power loss of IGBT, FWD and half bridge, respectively. The meaning of thermal impedances is shown in Fig. 4(a).

However, the coolant temperature is strongly influenced by the flow rate of coolant, and the corresponding thermal impedance $Z_{thjf\_IGBT}(t)$ and $Z_{thif\_FWD}(t)$ should be adjusted when the flow rate changes, which means the thermal impedance curve of different flow rates should be obtained via large experimental calibration. The measurement process is complicated and leads to larger cost pressure. Under the LR and ASC conditions, the coolant flow rate is often changed to accelerate the heat dissipation, so the traditional Foster model may not suitable for abnormal condition.

B. PROPOSED THERMAL MODEL

In this paper, a modified Foster thermal model based on NTC temperature sensor is proposed, as shown in Fig. 4(b). By comparing the two modeling methods, it can be found that the difference is whether to choose the coolant as the reference point. The mathematical model of proposed thermal model is expressed as:

$$\begin{aligned} T_{jIGBT}(t) &= T_{NTC}(t) + Z_{thjn\_IGBT}(t)\,P_{IGBT}(t) \\ &\quad + Z_{th\_DCI}(t)\,P_{FWD}(t) \\ T_{jFWD}(t) &= T_{NTC}(t) + Z_{thjn\_FWD}(t)\,P_{IGBT}(t) \\ &\quad + Z_{th\_ICD}(t)\,P_{IGBT}(t) \end{aligned} \tag{22}$$

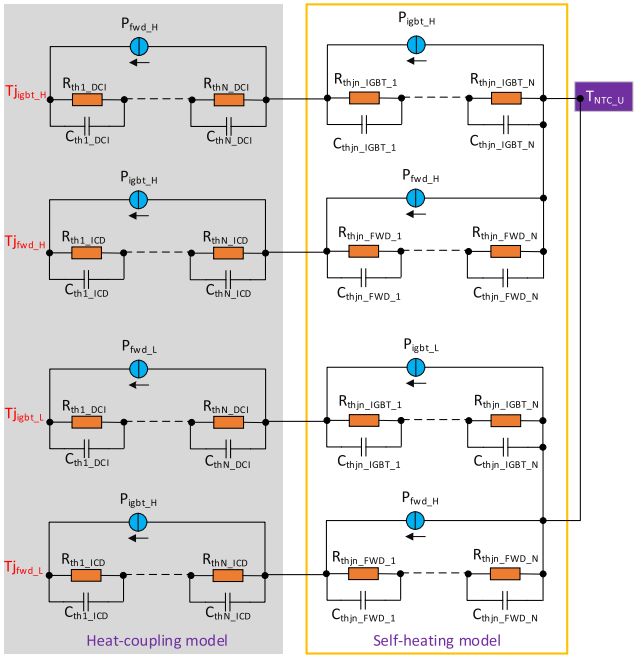

FIGURE 5. Proposed thermal model of IGBT half - bridge module.

Fig. 5 shows the proposed thermal model of IGBT half - bridge module, including the self-heating model and the heat-coupling model. Due to the series property of Foster model, the sub-equivalent model can be connected in series to form the half-bridge thermal model. Furthermore, the constant current source modules represent the power loss. P_{igbt_H}, P_{igbt_L}, P_{fwd_L} and P_{fwd_L} are the power loss of upper switches and lower switches of IGBT and FWD, respectively. All the parameters of thermal resistance and thermal capacity are fitted according to cooling curves obtained from experimental results and have nothing to do with the actual physical heat transfer process.

C. IDENTIFICATION OF THE PARAMETERS OF THE PROPOSED MODEL

1) MEASUREMENT OF THE THERMAL IMPEDANCE

A common measurement method for thermal impedance is to heat the measured object to a steady state using the heating

source with constant power, then remove the heating source and record the cooling curve. According to the definition of thermal impedance as shown in (23), the data of (t, $Z_{th}(t)$) can be obtained. The larger the sampling frequency of the cooling curve is, the higher the precision of the fitting Foster model will be. The order n of Foster model can be selected according to the practical need. Generally, the higher the order is, the higher the accuracy is. In practical engineering application, the compromise will be carried on considering the accuracy and the computation quantity.

$$Z_{th}(t) = \frac{T_j(t) - T_j(0)}{P(const)} \tag{23}$$

where $T_j(0)$ represents the initial temperature; $T_j(t)$ is the cooling curve, and $P(const)$ represents the power of the heating source.

The measurement method based on TSEP is adopted in this paper, since it can get more thermal impedance data with a faster dynamic response. This method obtains the junction temperature indirectly by measuring the on-state voltage $V_{ce}\left(V_{fd}\right)$. Especially when the current is small (usually 1/1000 of the rated current), $V_{ce}(V_{fd})$ is linear to the temperature [10]. The formula of the junction temperature calibration curve is as follows.

$$\begin{aligned} V_{ce}(T) &= k_{igbt}T + b_{igbt} \\ V_{fd}(T) &= k_{fwd}T + b_{fwd} \end{aligned} \tag{24}$$

As for the proposed thermal model, four thermal capacitances $Z_{thjn\_IGBT}(t)$, $Z_{thjn\_FWD}(t)$, $Z_{th\_ICD}(t)$ and $Z_{th\_DCI}(t)$ should be measured.

$Z_{thjn\_IGBT}(t)$ and $Z_{thjn\_FWD}(t)$ can be obtained via the cooling curve. However, different from the measurement of $Z_{thjf\_IGBT}(t)$ and $Z_{thif\_FWD}(t)$, the experiment can only fix the coolant temperature but not the NTC temperature. Therefore, it is necessary to measure the cooling curve of IGBT(FWD) and NTC at the same time, and it can be expressed by the following formulas.

$$\begin{aligned} &Z_{thjn\_IGBT}(t) \\ &= \frac{\left(T_{j\_IGBT}(t) - T_{j\_IGBT}(0)\right) - \left(T_{NTC}(t) - T_{j\_IGBT}(0)\right)}{P_{IGBT}(const)} \\ &= \frac{T_{j\_IGBT}(t) - T_{NTC}(t)}{P_{IGBT}(const)} \end{aligned} \tag{25}$$

$$\begin{aligned} &Z_{thjn\_FWD}(t) \\ &= \frac{\left(T_{j\_FWD}(t) - T_{j\_FWD}(0)\right) - \left(T_{NTC}(t) - T_{j\_FWD}(0)\right)}{P_{FWD}(const)} \\ &= \frac{T_{j\_FWD}(t) - T_{NTC}(t)}{P_{FWD}(const)} \end{aligned} \tag{26}$$

where $T_{j\_IGBT}(t)$, $T_{NTC}(t)$, $T_{j\_FWD}(t)$ represent the cooling curve of IGBT, NTC and FWD, respectively; $T_{j\_IGBT}(0)$ and $T_{j\_FWD}(0)$ represent the initial temperature of IGBT and FWD, respectively; $P_{IGBT}(const)$ and $P_{FWD}(const)$ represent the power of heating source for IGBT, FWD, respectively.

In respect to the measurement of thermal coupling impedance, take $Z_{th\_ICD}(t)$ for example, the IGBT is heated and then remove the heat source. The cooling curve of FWD is recorded and the measurement of the coupling thermal impedance is shown in (27). Similarly, $Z_{th\_DCI}(t)$ can be obtained according to (28).

$$Z_{th\_ICD}(t) = \frac{T_{j\_FWD}(0) - T_{j\_FWD}(t)}{P_{IGBT}(const)} \tag{27}$$

$$Z_{th\_DCI}(t) = \frac{T_{j\_IGBT}(0) - T_{j\_IGBT}(t)}{P_{FWD}(const)} \tag{28}$$

It should be noted that $Z_{th\_ICD}(t)$ is the same as $Z_{th\_DCI}(t)$, since the thermal coupling shares the same coupling path.

2) IDENTIFICATION OF RESISTANCE AND CAPACITANCE OF PROPOSED MODEL

After obtaining the thermal impedance through the cooling curve, the least square method is adopted to fit the resistance and capacitance of the proposed thermal model based on (30).

The Foster model is the series of RC parallel sub-network and can be expressed as:

$$Z_{th}(s) = \sum_{i=1}^{n} \frac{R_{thi}}{1 + R_{thi}C_{thi}s} \tag{29}$$

where $Z_{th}(s)$ represents the thermal impedance of n-order thermal model. R_{thi} and C_{thi} are the resistance and capacitance of RC parallel sub-network, respectively.

Equation (29) can be also expressed as:

$$Z_{th}(t) = \sum_{i=1}^{n} R_{thi}\left(1 - e^{-\frac{t}{\tau_i}}\right) \tag{30}$$

where τ_i represents time constant and can be calculated as:

$$\tau_i = R_{thi}C_{thi} \tag{31}$$

Generally, the compromise will be carried on considering the fitting accuracy and the computation burden.

D. DISCRETIZATION OF PROPOSED MODEL

In order to realize the on-line junction temperature estimation, the model needs to be discretized. The Foster model is the series of RC parallel sub-network, so only the discretization of RC parallel sub-network needs to be considered. The transfer function of RC parallel sub-network is expressed as follows.

$$G_{RC}(s) = \frac{R_{th}}{1 + sR_{th}C_{th}} \tag{32}$$

The discretization of (32) using Backward Euler is calculated as

$$G_{RC}(z) = \frac{\Delta T(z)}{P(z)} = \frac{R_{th}}{1 + \frac{1-z^{-1}}{T_s}R_{th}C_{th}} \tag{33}$$

Equation (39) can be written as a difference form.

$$\Delta T(k) = \frac{R_{th}T_s}{T_s + R_{th}C_{th}}P(k) + \frac{R_{th}C_{th}}{T_s + R_{th}C_{th}} \times \Delta T(k-1) \tag{34}$$

where T_s is the discrete sampling time.

For the n-order Foster thermal model, the discrete junction temperature can be expressed as follows.

$$T_j(k) = T_{NTC}(k) + \sum_{i=1}^{n}\left(\frac{R_{thi}T_s}{T_s + R_{thi}C_{thi}}P(k) + \frac{R_{thi}C_{thi}}{T_s + R_{thi}C_{thi}}\Delta T_i(k-1)\right) \quad (35)$$

IV. EXPERIMENTAL VERIFICATION OF IGBT JUNCTION TEMPERATURE ESTIMATION

Since the focus of this paper is on the IGBT, not on the free-wheeling diode, so the results of the junction temperature prediction for free-wheeling diode are not presented in the experiment.

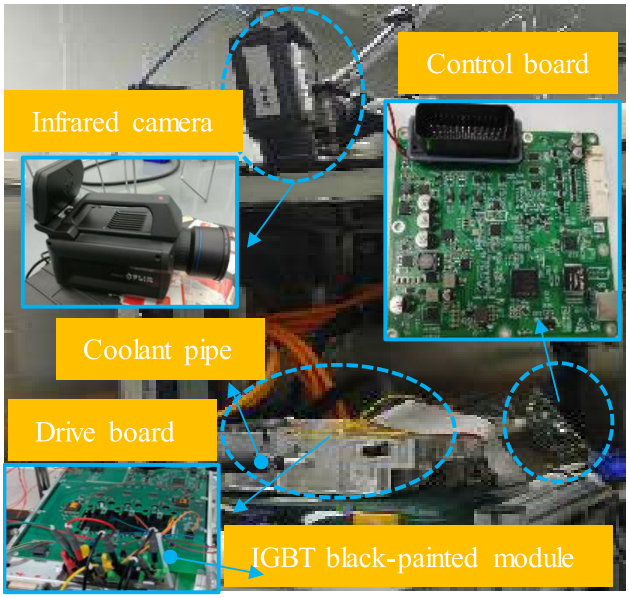

FIGURE 6. Test bench of real-time junction temperature measurement.

A. EXPERIMENT SET UP

IGBT junction temperature estimation is experimentally validated via the inverter with black-painted module in the motor test bench. By introducing the black-painted module, the junction temperature can be tested by the infrared camera with the sampling frequency of 200Hz. The online junction temperature estimation from the proposed thermal model will be compared with the results from the black-painted module. Fig. 6 shows the test bench of real-time junction temperature measurement. Fig. 7 illustrates the principle block diagram of experimental measurement. The parameters of PMSM used in the test are shown in Table 1. The Infineon HP-Drive IGBT module is selected to validate the proposed thermal model.

B. COMPARISON OF THE THERMAL IMPEDANCE UNDER DIFFERENT FLOW RATES

The steady-state thermal impedances of the traditional model and the proposed model are compared as shown in Fig.8 and Fig. 9. Under different flow rates, Fig. 8 illustrates the comparison of thermal impedances Z_{thjf_IGBT} and Z_{thjn_IGBT}, and Fig. 10 shows the comparison of steady-state thermal impedances Z_{thjf_FWD} and Z_{thjn_FWD}.

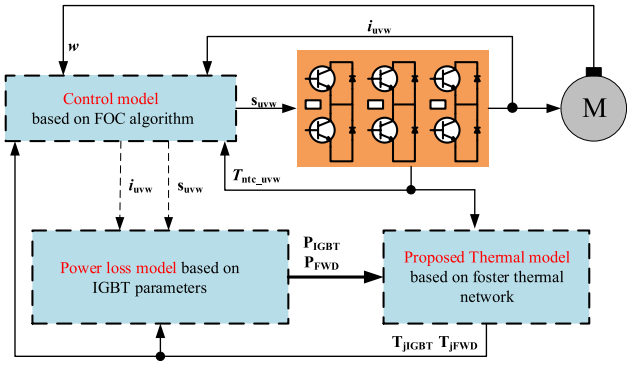

FIGURE 7. Block diagram of junction temperature estimation of IGBT.

TABLE 1. PMSM parameters.

Symbol	Quantity	Value
ψ	magnetic flux	0.062 Wb
L_d	direct axis inductance	0.000105 H
L_q	quadrature axis inductance	0.000252 H
R_s	stator resistance	0.012 Ω
J	rotational inertia	0.12 kg· m^2
p	pole pairs	4

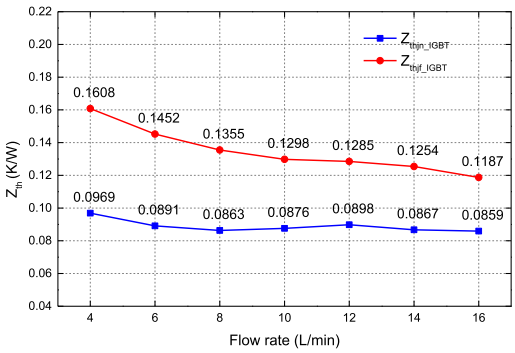

FIGURE 8. Steady-state thermal impedances of Z_{thjf_IGBT} and Z_{thjn_IGBT} under different flow rates.

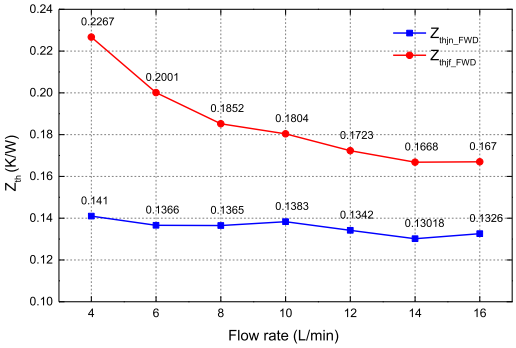

FIGURE 9. Steady-state thermal impedances of Z_{thjf_FWD} and Z_{thjn_FWD} under different flow rates.

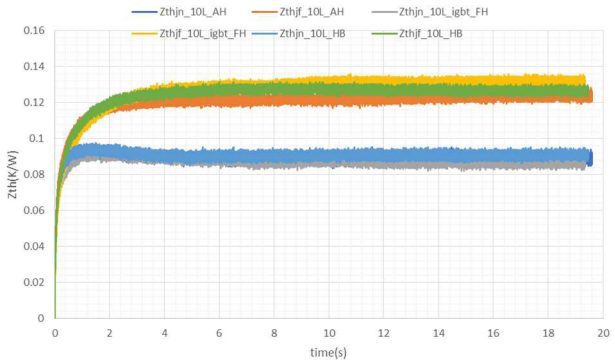

FIGURE 10. Thermal impedances of Z_{thjf_IGBT} and Z_{thjn_IGBT} at flow rate 10L/min.

It can be seen from Fig. 8 and Fig. 9 that Z_{thjf_IGBT} and Z_{thjf_FWD} of the traditional model are seriously affected by the flow rates, whereas Z_{thjn_IGBT} and Z_{thjn_FWD} of the proposed model are basically constant. The comparison shows that the thermal impedances between the NTC and IGBT(FWD) are independent of the flow rates, which means there is no need to change the thermal impedance in real time according to the flow rate with respect to the proposed thermal model.

It should be noted that the coupling thermal impedance Z_{th_ICD} and Z_{th_DCI} are not compared, since there is no difference between the traditional model and the proposed model in terms of coupling thermal impedance.

C. MEASUREMENT OF RESISTANCE AND CAPACITANCE OF THE PROPOSED MODEL

A common flow rate 10L/min is selected to conduct the temperature prediction validation. The resistances and capacitances of the proposed thermal model are fitted by means of the thermal impedance curves. Considering the fitting accuracy and computation pressure, Z_{thjn_IGBT} and Z_{thjn_FWD} are expressed by 4-order RC-network, while Z_{th_ICD} and Z_{th_DCI} are described by 3-order RC-network.

Fig. 10 shows the comparison of three different heating methods: IGBT tubes of the upper switch in a half bridge are heated indicted by thermal impedance $Z_{thjf\_10L\_AH}$ and $Z_{thjn\_10L\_AH}$; IGBT tubes of the half bridge are heated indicted by thermal impedance $Z_{thjf\_10L\_HB}$ and $Z_{thjn\_10L\_HB}$; IGBT tubes of the full bridge are heated indicted by thermal impedance $Z_{thjf\_10L\_igbt\_FH}$ and $Z_{thjn\_10L\_igbt\_FH}$.

It can be seen that Z_{thjn_IGBT} changes slightly under different heating methods, whereas the change of Z_{thjf_IGBT} is a little large. This result shows the convenience of thermal impedance measurement using the proposed method. The method of full-bridge heating is adopted to measure the thermal impedance Z_{thjn_IGBT}, the values of resistance and capacitance are listed in Table 2.

Since Fig.10 shows the weakness of IGBT thermal impedance measurement in terms of traditional Foster model, it is not necessary to make a comparison between Z_{thjn_FWD} and Z_{thjf_FWD}. Fig.11 illustrates the comparison of two

TABLE 2. Parameters of Z_{thjn_IGBT}.

resistance	value	capacitance	value	Time constant	value
R_1	0.00108	C_1	335.30	Tau_1	0.3628
R_2	0.00878	C_2	60.77	Tau_2	0.5333
R_3	0.04082	C_3	1.90	Tau_3	0.0775
R_4	0.04082	C_4	1.86	Tau_4	0.0758

different heating methods for the measurement of Z_{thjn_FWD} and it shows little difference between full-bridge heating and single tube heating.

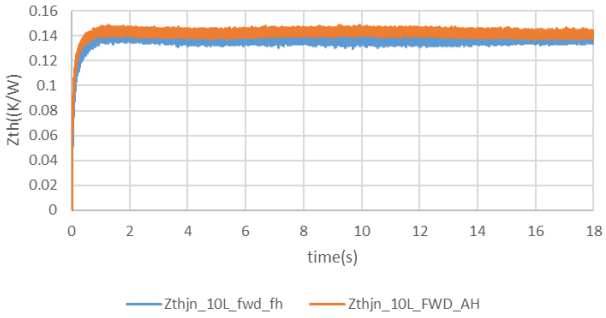

FIGURE 11. Thermal impedances of Z_{thjn_FWD} at the flow rate 10L/min.

Similar to the measurement of Z_{thjn_IGBT}, the method of full-bridge heating is adopted to measure the thermal impedance Z_{thjn_FWD} and the values of resistance and capacitance are listed in Table 3.

TABLE 3. Parameters of Z_{thjn_FWD}.

resistance	value	capacitance	value	Time constant	value
R_1	0.07105	C_1	0.6083	Tau_1	0.0432
R_2	0.05410	C_2	4.4214	Tau_2	0.2392
R_3	0.00100	C_3	251.50	Tau_3	0.2515
R_4	0.01145	C_4	0.1299	Tau_4	0.0015

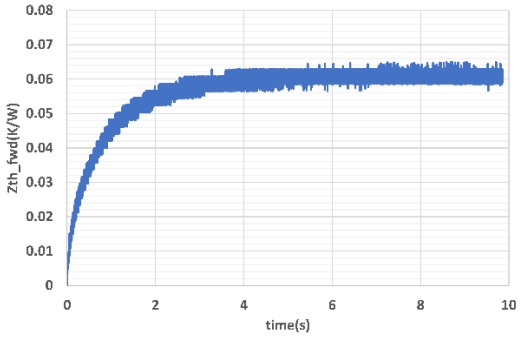

FIGURE 12. Thermal impedances of Z_{th_ICD} and Z_{th_DCI} at the flow rate 10L/min.

The thermal impedance curve of $Z_{th\_ICD}(t)$ is the same as $Z_{th\_DCI}(t)$, since the thermal coupling shares the same coupling path. Fig.12 shows the thermal impedance curve of

TABLE 4. Parameters of Z_{th_ICD} and Z_{th_DCI}.

resistance	value	capacitance	value	Time constant	value
R_1	0.031	C_1	40.774	Tau_1	1.264
R_2	0.021	C_2	19.348	Tau_2	0.406
R_3	0.010	C_3	2.913	Tau_3	0.0293

Z_{th_ICD} and Z_{th_DCI}, and the measurement method is introduced in the part C of Section III. The values of resistances and capacitances are shown in Table 4.

D. IGBT JUNCTION TEMPERATURE VERIFICATION UNDER LOCKED-ROTOR CONDITION

The verification is conducted under the following condition: 10kHz switching frequency, 400V bus voltage, and 10L/min flow rate. The power loss is calculated according to the formulas in Section II and the calculation accuracy of power loss is verified by the junction temperature estimation results. The junction temperature verification is based on black-painted module. The results of IGBT power losses and the junction temperature estimation are shown in Fig. 13.

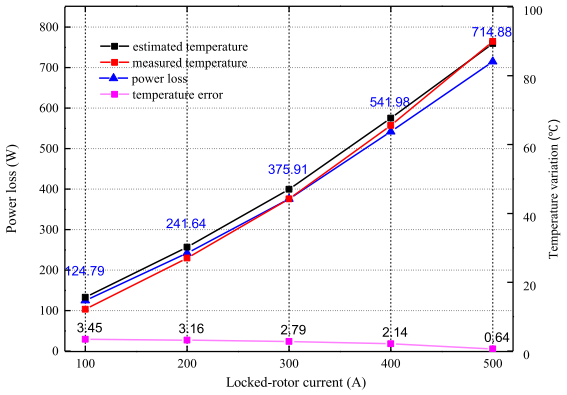

FIGURE 13. Power loss and junction temperature variation of IGBT under different locked-rotor currents.

When the locked-rotor current reaches 500A, the IGBT loss is 715W and the temperature rise has reached around 90°C. According to the worst-case analysis, assuming that the coolant temperature is 65°C, the IGBT junction temperature has reached 155°C. However, to avoid the risk of IGBT overheating, the real-time junction temperature should not exceed 150°C. Thus, the rocked-rotor current of HP-drive should be set less than 500A when the flow rate is 10L/min.

Fig. 13 compares the results of the estimated junction temperature with the measured values. The average estimation accuracy is about 3°C, and the estimation accuracy is more accurate under the condition of the large current, since the conduction loss of the large current is relatively large.

Fig. 14 illustrates the results of thermal infrared camera under the experimental condition: 550A locked-rotor current, 10L/min flow rate, and coolant temperature 20°C. From the perspective of the thermal stress distribution field, IGBT of upper switches and FWD of lower switches are hotter, which

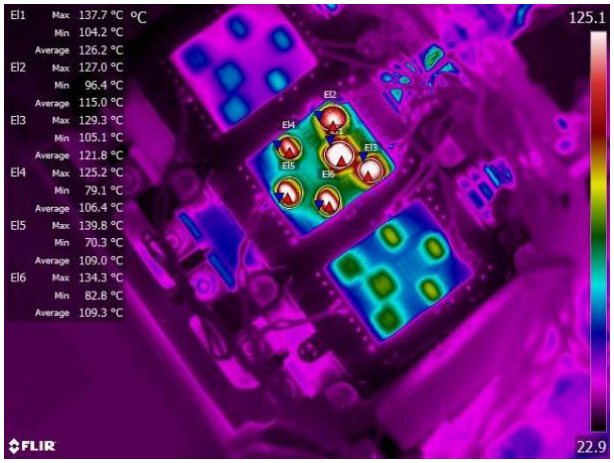

FIGURE 14. The results of thermal infrared camera under the 550A locked-rotor current.

is consistent with the theoretical analysis, since IGBT of upper switches and FWD of lower switches are in the working condition of zero voltage vector U111 and U000 for a long time.

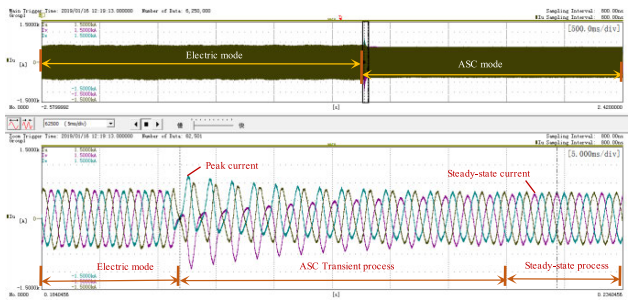

FIGURE 15. Three-phase current waveform under ASC condition.

E. IGBT JUNCTION TEMPERATURE VERIFICATION UNDER ASC CONDITION

Fig. 15 shows the measured three-phase current waveform during ASC execution in motor test bench. At first, the motor works in electric mode at the speed of 8000rpm and the load torque of 185N. The steady-state current amplitude is about 615A. After switching to ASC mode, the current increases to 1080A in a short time, and then enters the steady state.

Since the duration of transient process is short, the temperature verification is not easy to be conducted in test bench and only depends on PSPICE simulation. Thus, the junction temperature verification includes the transient and steady-state process.

1) ASC ELECTROTHERMAL TRANSISENT SIMULATION

Assuming that the coolant temperature is 65°C and the flow rate is 10L/min, the junction temperature of IGBT in ASC mode is simulated by PSPICE model. As can be seen from Fig. 16, in the early stage of active short circuit, the peak current is at 1120A. Due to the fast decay of transient components and the existence of IGBT module heat capacity,

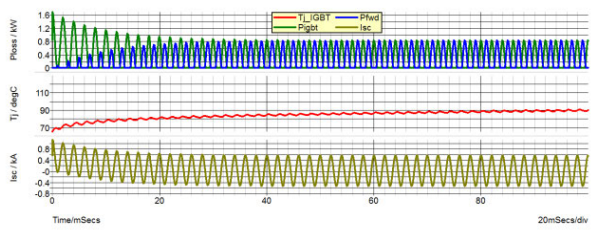

FIGURE 16. IGBT thermal stress simulation analysis for ASC transient process.

the transient peak current does not cause the rapid IGBT junction temperature rise. In fact, IGBT temperature increases rapidly in the initial stage. However, due to the rapid attenuation of peak current, when IGBT temperature increases to 90°C, the transient component of active short circuit current becomes weak and the ASC mode enters the steady-state process.

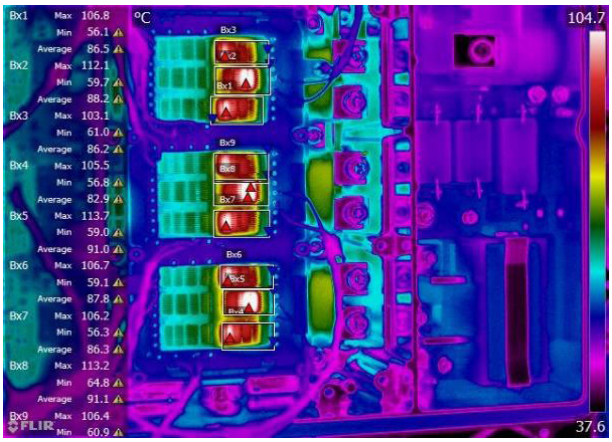

FIGURE 17. The results of thermal infrared camera under ASC mode.

2) ONLINE STEADT-STATE JUNCTION TEMPERATURE ESTIMATION

Fig. 17 is the results of the thermal infrared camera of the IGBT module when the motor enters the steady state of ASC mode. It can be seen that only half part of IGBT module is operating.

In the on-line junction temperature validation experiment, the coolant temperature is changed to 25°C. As can be seen from Fig. 18, the PMSM is put into the normal electric mode from 0.6s to 2.7s with the load torque of 60Nm and the speed of 8000rpm. The motor enters ASC mode at 2.7s, and the duration of ASC mode is about 1s. The loss of IGBT is 176W and the corresponding junction temperature is about 50°C.

It can be seen that the measured value can predict the real-time junction temperature variation and the error is within 3°C. The corresponding temperature variation is 25°C, which is consistent with the temperature rise of simulation results with the 65°C coolant temperature and 90°C IGBT junction temperature.

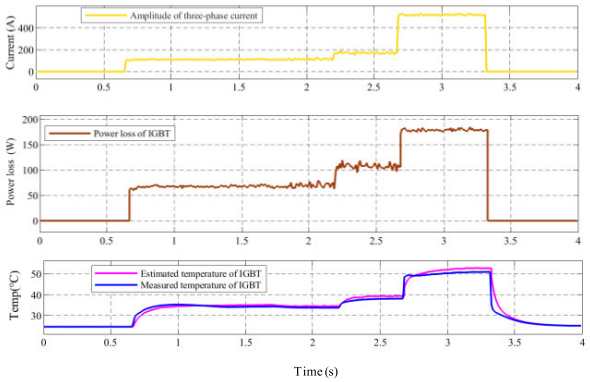

FIGURE 18. Real-time calculation of IGBT junction temperature under ASC mode.

It can be found that the response of the estimated temperature is slower than that of the measured temperature. This is because the values of resistance and capacitance obtained by the fitting the measured thermal impedance are not accurate enough to describe the dynamic process, that is, there are some deviations in the fitting operation. Furthermore, there are also some errors during the measurement of thermal impedance. So the predicted temperature cannot track the temperature change totally with some delay when the power loss changes. However, the delay is not serious and we pay more attention to the steady-state values. The accuracy of steady-state shows good prediction effect and the estimation error is below 3°C.

V. CONCLUSION

In this paper, a modified foster thermal model based on NTC temperature sensor has been proposed under the LR and ASC conditions. Compared with the traditional Foster model, the proposed thermal model is proved to be independent of the coolant flow rates, which shows its advantages without complex calibration of thermal impedance under different flow rates.

The proposed thermal model has been validated by experiments. With respect to locked-rotor condition, the temperature performance is indicated with the average estimation error of about 3°C under different locked-rotor currents; Offline simulation and experimental measurement are performed to verify the correctness and effectiveness of the proposed thermal model under ASC condition. The offline simulation shows that the transient peak current does not cause the rapid IGBT junction temperature rise. The steady-state experiment is conducted to validate the proposed model with small estimation error. It can be concluded that active junction temperature control is supposed to work when the predicted junction temperature is beyond the safety threshold under the LR and ASC condition..

REFERENCES

[1] I. Aranzabal, I. M. de Alegria, N. Delmonte, P. Cova, and I. Kortabarria, "Comparison of the heat transfer capabilities of conventional single- and two-phase cooling systems for an electric vehicle IGBT power module," *IEEE Trans. Power Electron.*, vol. 34, no. 5, pp. 4185–4194, May 2019, doi: 10.1109/TPEL.2018.2862943.

[2] X. Wang, Z. Li, F. Yao, and S. Tang, "Simplified estimation of junction temperature fluctuation at the fundamental frequency for IGBT modules considering mission profile," *IEEE Access*, vol. 7, pp. 149308–149317, 2019, doi: 10.1109/ACCESS.2019.2947346.

[3] B. Wang, L. Zhou, Y. Zhang, K. Wang, X. Du, and P. Sun, "Active junction temperature control of IGBT based on adjusting the turn-off trajectory," *IEEE Trans. Power Electron.*, vol. 33, no. 7, pp. 5811–5823, Jul. 2018, doi: 10.1109/TPEL.2017.2749383.

[4] J. Zhou, B. Li, Y. He, W. Yuan, J. Liu, and H. Ni, "Electro-thermal-mechanical multiphysics coupling failure analysis based on improved IGBT dynamic model," *IEEE Access*, vol. 7, pp. 174155–174166, 2019, doi: 10.1109/ACCESS.2019.2956186.

[5] Z. Wang, B. Tian, W. Qiao, and L. Qu, "Real-time aging monitoring for IGBT modules using case temperature," *IEEE Trans. Ind. Electron.*, vol. 63, no. 2, pp. 1168–1178, Feb. 2016, doi: 10.1109/TIE.2015.2497665.

[6] A. S. Bahman, F. Iannuzzo, C. Uhrenfeldt, F. Blaabjerg, and S. Munk-Nielsen, "Modeling of short-circuit-related thermal stress in aged IGBT modules," *IEEE Trans. Ind. Appl.*, vol. 53, no. 5, pp. 4788–4795, Sep. 2017, doi: 10.1109/TIA.2017.2702594.

[7] N. Baker, S. Munk-Nielsen, F. Iannuzzo, and M. Liserre, "IGBT junction temperature measurement via peak gate current," *IEEE Trans. Power Electron.*, vol. 31, no. 5, pp. 3784–3793, May 2016, doi: 10.1109/TPEL.2015.2464714.

[8] L. Dupont and Y. Avenas, "Preliminary evaluation of thermo-sensitive electrical parameters based on the forward voltage for online chip temperature measurements of IGBT devices," *IEEE Trans. Ind. Appl.*, vol. 51, no. 6, pp. 4688–4698, Nov. 2015, doi: 10.1109/TIA.2015.2458973.

[9] N. Baker and F. Iannuzzo, "The temperature dependence of the flatband voltage in high-power IGBTs," *IEEE Trans. Ind. Electron.*, vol. 66, no. 7, pp. 5581–5584, Jul. 2019, doi: 10.1109/TIE.2018.2854568.

[10] M. A. Eleffendi and C. M. Johnson, "Application of Kalman filter to estimate junction temperature in IGBT power modules," *IEEE Trans. Power Electron.*, vol. 31, no. 2, pp. 1576–1587, Feb. 2016, doi: 10.1109/TPEL.2015.2418711.

[11] H. Luo, Y. Chen, P. Sun, W. Li, and X. He, "Junction temperature extraction approach with turn-off delay time for high-voltage high-power IGBT modules," *IEEE Trans. Power Electron.*, vol. 31, no. 7, pp. 5122–5132, Jul. 2016, doi: 10.1109/TPEL.2015.2481465.

[12] Z. Xu, F. Xu, and F. Wang, "Junction temperature measurement of IGBTs using short circuit current as a temperature sensitive electrical parameter for converter prototype evaluation," *IEEE Trans. Ind. Electron.*, vol. 62, no. 6, pp. 3419–3429, Jun. 2015, doi: 10.1109/TIE.2014.2374575.

[13] Z. Wang and W. Qiao, "An online frequency-domain junction temperature estimation method for IGBT modules," *IEEE Trans. Power Electron.*, vol. 30, no. 9, pp. 4633–4637, Sep. 2015, doi: 10.1109/TPEL.2015.2397955.

[14] R. Wu, H. Wang, K. B. Pedersen, K. Ma, P. Ghimire, F. Iannuzzo, and F. Blaabjerg, "A temperature-dependent thermal model of IGBT modules suitable for circuit-level simulations," *IEEE Trans. Ind. Appl.*, vol. 52, no. 4, pp. 3306–3314, Jul. 2016, doi: 10.1109/TIA.2016.2540614.

[15] A. S. Bahman, K. Ma, and F. Blaabjerg, "A lumped thermal model including thermal coupling and thermal boundary conditions for high-power IGBT modules," *IEEE Trans. Power Electron.*, vol. 33, no. 3, pp. 2518–2530, Mar. 2018, doi: 10.1109/TPEL.2017.2694548.

[16] N. Baker, L. Dupont, S. Munk-Nielsen, F. Iannuzzo, and M. Liserre, "IR camera validation of IGBT junction temperature measurement via peak gate current," *IEEE Trans. Power Electron.*, vol. 32, no. 4, pp. 3099–3111, Apr. 2017, doi: 10.1109/TPEL.2016.2573761.

[17] L. Peng, D. Gao, W. Shen, and H. Yan, "IGBT junction temperature estimation in water cooling power modules," in *Proc. IEEE Int. Power Electron. Appl. Conf. Expo. (PEAC)*, Nov. 2018, pp. 1–6.

[18] X. Du, J. Zhang, S. Zheng, and H.-M. Tai, "Thermal network parameter estimation using cooling curve of IGBT module," *IEEE Trans. Power Electron.*, vol. 34, no. 8, pp. 7957–7971, Aug. 2019, doi: 10.1109/TPEL.2018.2879845.

[19] J. Zhang, X. Du, Y. Yu, S. Zheng, P. Sun, and H.-M. Tai, "Thermal parameter monitoring of IGBT module using junction temperature cooling curves," *IEEE Trans. Ind. Electron.*, vol. 66, no. 10, pp. 8148–8160, Oct. 2019, doi: 10.1109/TIE.2018.2883258.

[20] W. Zhihong, S. Xiezu, and Z. Yuan, "IGBT junction and coolant temperature estimation by thermal model," *Microelectron. Rel.*, vol. 87, pp. 168–182, Aug. 2018, doi: 10.1016/j.microrel.2018.06.018.

[21] K. Lu, Y. Zhu, Z. Wu, and M. Xiao, "Suppression of current fluctuations and the brake torque for PMSM shutoff in electric vehicles," *Math. Problems Eng.*, vol. 2019, pp. 1–13, Sep. 2019, doi: 10.1155/2019/5026316.

[22] W. Bailey, Q. Zhang, I. Falorio, J. Pelegrin, and Y. Yang, "Locked rotor and transient tests of a 100 kW HTS machine," *IEEE Trans. Appl. Supercond.*, vol. 27, no. 4, pp. 1–5, Jun. 2017, doi: 10.1109/TASC.2017.2671683.

[23] G. Xie, Y. Chen, Y. Liu, R. Li, and K. Li, "Minimizing development cost with reliability goal for automotive functional safety during design phase," *IEEE Trans. Rel.*, vol. 67, no. 1, pp. 196–211, Mar. 2018, doi: 10.1109/TR.2017.2778070.

[24] C. Tao, "Functional safety concept design of hybrid electric vehicle following ISO 26262," in *Proc. IEEE Conf. Expo Transp. Electrific. Asia–Pacific (ITEC Asia–Pacific)*, Aug. 2014, pp. 1–6.

[25] R. McElveen and M. Melfi, "Locked-rotor test methods for induction motors investigated," *IEEE Trans. Ind. Appl.*, vol. 52, no. 4, pp. 3595–3602, Jul. 2016, doi: 10.1109/TIA.2016.2544925.

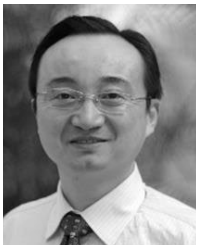

YUAN ZHU received the B.S. and Ph.D. degrees in automotive engineering from Tsinghua University, Beijing, China, in 1998 and 2003, respectively. Since 2005, he has been an Associate Professor with Tongji University, Shanghai, China, and the Executive Director of the Tongji-Vector Automotive Technology Joint Laboratory. His research interests include the electrical drive system of new energy vehicles, perception algorithm for autonomous vehicles, and functional safety.

MINGKANG XIAO received the B.S. degree in automotive engineering from the Wuhan University of Technology, Wuhan, China, in 2017. He is currently pursuing the Ph.D. degree in automotive engineering with the School of Automotive Studies, Tongji University, Shanghai, China. His research interests include the reliability of power electronics and sensorless control algorithm of high-speed PMSM in new energy vehicles.

XIEZU SU received the B.S. degree in measurement technology and instrument from the Huazhong University of Science and Technology, Wuhan, China, in 2008, the M.S. degree in control theory and control engineering from Zhejiang University, Hangzhou, China, in 2011, and the Ph.D. degree in automotive engineering from the School of Automotive Studies, Tongji University, Shanghai, China, in 2020. His research interest includes the reliability of power electronics in new energy vehicles.

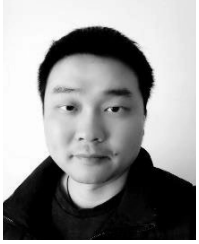

KE LU received the B.S. degree in automation and the M.S. and Ph.D. degrees in computer science and automotive engineering from Tongji University, Shanghai, China, in 2006, 2009, and 2018, respectively. He is currently an Engineer with the School of Automotive Studies, Tonji University. His main research interests include motor control for electric vehicles, perception algorithm for autonomous vehicles, and functional safety.

ZHIHONG WU (Member, IEEE) received the B.S. and M.S. degrees in electrical engineering from Zhejiang University, Hangzhou, China, in 1982 and 1988, respectively, and the Ph.D. degree from the Technical University of Berlin, Berlin, Germany, in 1999.

He is currently a Professor with the School of Automotive Studies, Tonji University, the Deputy Dean of the Sino-German College for Postgraduate Studies, Tongji University, the Infineon Endowed Chair Professor of embedded systems, and the Director of the Infineon-Tongji Automotive Electronics Joint Laboratory and the Tongji-Vector Automotive Technology Joint Laboratory. His research interests include the electrical drive system of new energy vehicles, perception algorithm for autonomous vehicles, and functional safety. He is a member of the Board of Director of the Power Converter and Intelligent Motion (PCIM) Asia and the International Science Committee of European Power Electronics (EPE) and the Vice Chairman of the Shanghai Power Supply Association.

GANG YANG received the B.S. degree in automotive engineering from Tsinghua University, Beijing, China, in 2019. He is currently pursuing the M.S. degree in control theory and control engineering with Tongji University, Shanghai, China. His research interests include high-speed position sensorless drive in PMSM and parameter identification.